*Article*

# Thermal-Hydraulic Modeling of Oil-Immersed Motor Pump

Junqiang Shi [1], Ziyang Li [2], Jingcheng Gao [1], Dongjing Chen [2], Xiaotao Li [1], Ying Li [2,3,4], Jin Zhang [2,3,4,5,]* and Xiangdong Kong [2,3,4]

1  Beijing Machinery Industry Automation Research Institute Co., Ltd., Beijing 100120, China; shijq@riamb.ac.cn (J.S.); gaojch@riamb.ac.cn (J.G.); lixt@riamb.ac.cn (X.L.)
2  College of Mechanical Engineering, Yanshan University, Qinhuangdao 066004, China; lziyang@stumail.ysu.edu.cn (Z.L.); chendj@stumail.ysu.edu.cn (D.C.); yingli@ysu.edu.cn (Y.L.); xdkong@ysu.edu.cn (X.K.)
3  Hebei Provincial Key Laboratory of Heavy Machinery Fluid Power Transmission and Control, Qinhuangdao 066004, China
4  National & Local Joint Engineering Research Center for Advanced Manufacture Forming Technology and Equipment, Qinhuangdao 066004, China
5  China Key Laboratory of Advanced Forging & Stamping Technology and Science, Yanshan University, Qinhuangdao 066004, China
*  Correspondence: zhangjin@ysu.edu.cn

**Abstract:** The integrated design of the motor and axial piston pump eliminates the coupling structure, resulting in a compact and lightweight motor-pump structure. The challenge of motors overheating has always been a major concern. To address this issue, the hydraulic oil throughout the motor pump is utilized for cooling the high-speed motor, effectively improving the power density and heat dissipation capability of the hydraulic power unit. This integrated design approach has successfully resolved the significant issue of overheating motors, leading to enhanced performance of the hydraulic power unit. To address this concern, the entire motor pump's oil is utilized to cool the high-speed motor. Consequently, the thermodynamic prediction of high-speed motor pumps has become increasingly important. In this study, the impact of motor heat generation on hydrodynamics is analyzed, and the heat transfer of the motor pump is investigated using the control volume method. Furthermore, thermodynamic models of hysteresis loss, eddy current loss, alternating current loss, churning loss, and throttling loss are established for the oil-immersed motor pump. The change in oil viscosity is also considered. The instantaneous temperature change rule of the oil within the oil-immersed motor pump is derived. Additionally, the influence of various working conditions such as pressure and speed on the temperature of the motor pump's key node is examined. The experimental results indicate the accuracy of the thermodynamic calculation, and the significant effect of motor loss on the leakage temperature.

**Keywords:** motor pump; thermal-hydraulic model; motor loss; temperature calculation; oil viscosity

## 1. Introduction

The oil-immersed motor pump is a novel electro-hydraulic integrated power unit comprising an axial piston pump and a motor, exhibiting remarkable advantages of high efficiency, compact size, high energy utilization rate, high power density, and extended lifespan. It constitutes the essential component of the rudder control system for future large airliners and advanced warplanes, and represents a critical technology for the realization of intelligent actuation of high-end equipment [1–3]. However, due to its high-speed operation, it generates considerable heat within a limited time [3]. A considerable percentage of aviation safety accidents, approximately 40%, are caused by hydraulic system malfunction. Abnormal temperature elevation in the aircraft's hydraulic system contributes to 15% to 20% of these incidents [4]. Therefore, it is crucial to establish a thermodynamic model of the oil-immersed motor pump to accurately analyze its temperature distribution, enhance

its heat transfer and dissipation capacity, and effectively lower the system temperature. The establishment of a thermodynamic model is deemed crucial for the accurate analysis of the temperature distribution, enhancement of the heat transfer and dissipation capacity, and effective reduction of the system temperature in the oil-immersed motor pump.

The 3D model diagram of the motor pump is presented in Figure 1, where the motor and pump are interconnected via a rotating axis. The cylinder block is driven by the motor to rotate, thereby enabling the piston cavity to perform the oil-draining and oil-absorbing action. The pump comprises several components, including the cylinder block, valve plate, piston, and slipper [5]. The motor is primarily composed of the stator, rotor, permanent magnet, and winding.
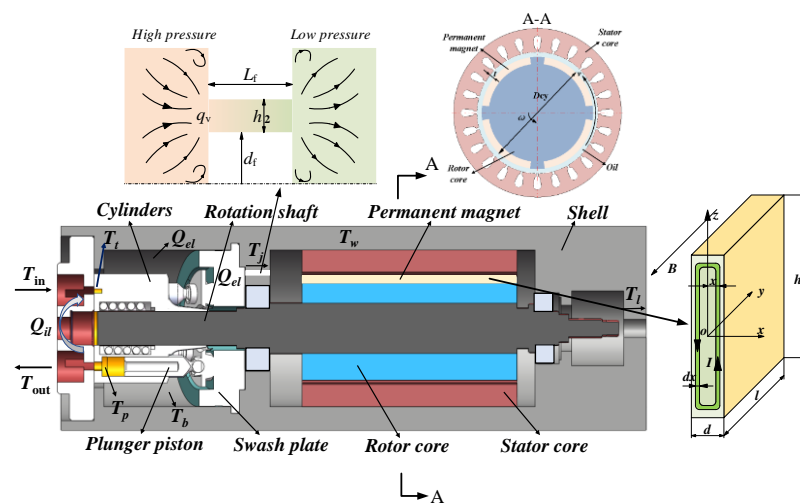


**Figure 1.** Structural diagram of motor pump.

The practical application of high-speed motor pumps has long been impeded by their thermal management. The heat generation in the piston pump is specifically attributed to the frictional forces between its sliding surfaces and the mixing losses arising from the interaction of the cylinder and piston assembly, which are the underlying causes of heat generation. Additionally, core loss is induced by the high-speed motor's alternating magnetic field during operation, and a significant amount of heat is generated by energizing the stator winding [6–9]. Failure to effectively manage the aforementioned heat sources can result in the hydraulic system's abnormal temperature rise; ultimately a failure of the hydraulic system is caused.

The heat generated by oil-immersed motor pumps is primarily derived from fluid energy loss and electromagnetic heat generation resulting from the winding current. Researchers from various countries have investigated the thermodynamics of oil-immersed motor pumps. Zhang et al. [10] examined high-speed pumps, analyzing their power loss mechanisms, and establishing churning loss and thermodynamic models that account for churning loss. Shi et al. [11] employed the control volume method to establish a thermodynamic simulation model of an axial piston pump, predicting the temperature rise in each node and optimizing the piston design. Jordan [12] proposed models of hysteresis and eddy current losses based on the mechanism of core loss generation, while Bertotti [13,14] built on this work by introducing additional loss. Gao et al. [15] constructed a mathematical model of the fluid and temperature field coupling solution for high-speed hydraulic pump motors using the finite volume method, deriving the temperature field distribution of motor pumps. Li et al. [16] analyzed the losses of motor pumps and introduced them into the flow field as heat sources, accurately predicting the motor temperature. Popescu et al. [17] directly fed electromagnetic losses into a collective parametric thermal model to obtain temperature distribution. Lu et al. [18] incorporated losses derived from copper loss models into a collective parameter model, comparing the results with finite element

method calculations, which displayed good experimental fit. Guo et al. [19] proposed the MTC analysis method of motors, integrating calculated loss into fluid analysis based on fluid–solid coupled heat transfer, and subsequently returning the calculated temperature back to the electromagnetic field. Amadou Tinni et al. [20] calculated component temperatures by plugging motor losses into a "lumped heat network". Wang et al. [21] simplified the space between the stator and rotor into a hollow cylinder to explore the temperature distribution of motor pumps. The thermodynamic model is commonly employed by scholars to compute the temperature of piston pumps. Similarly, for motor heating, a comparable calculation method is employed that incorporates the motor's losses. In the context of motor pump temperature computation, the utilization of computational fluid dynamics software through which the calculation nodes are fewer and the process is time-consuming is warranted.

This paper focuses on the oil-immersed motor pump as the research subject, and aims to analyze the power loss and heat generation mechanism of the motor. Through a thorough analysis of the heat transfer process within the oil-immersed motor pump, a thermodynamic model is established to investigate the variations in the internal temperature of the motor pump under different pressure and flow conditions, as well as to clarify the effect of motor loss on temperature. Finally, experimental validation is conducted to verify the accuracy of the proposed thermodynamic model.

## 2. Mathematical Analysis

### 2.1. Heat Generation Mechanism

The loss of stator and rotor resulting from the fluctuation of magnetic flux is commonly referred to as core loss. Bertotti conducted a comprehensive investigation on the origin and constituents of core loss and introduced the separation theory of core loss, which posits that core loss is composed of hysteresis loss, eddy current loss, and additional loss.

As shown in Figure 2, the variation in magnetic field within the iron core will trigger the induction of current.
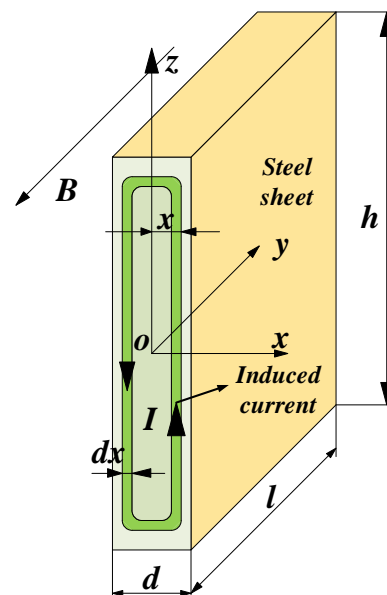


**Figure 2.** Schematic diagram of a steel sheet eddy current.

Based on Ohm's law and the law of electromagnetic induction, the power loss due to eddy currents, P, can be expressed as follows:

$$dp_b = \frac{E^2}{R} \tag{1}$$

where $R = \rho_1 \frac{2h}{ldx}$, $E = \sqrt{2}\pi f \phi$, $\phi = 2Bxh$.

By substituting the values of $R$, $E$ and $\phi$ into Equation (1), the expression for eddy current power loss $p_b$ can be derived.

$$dp_b = \int_0^{\frac{d}{2}} dp = \frac{4\pi^2 f^2 B^2 lh}{\rho_1} dx \tag{2}$$

Eddy current loss of the iron core $P_b$ as shown in Equation (3).

$$P_b = \frac{\pi^2}{6\rho_1}(fB)^2 d^3 lh \tag{3}$$

where $\rho_1$ is the resistivity of the core, $f$ is the frequency of the magnetic field, $B$ is the strength of the magnetic field.

The hysteresis loss is due to the hysteresis effect, and the hysteresis loss $P_h$ is shown in Equation (4).

$$P_h = \sigma_h f B^2 \tag{4}$$

The extra loss $P_{ex}$ is shown in Equation (5) [22].

$$P_{ex} = K_{ex}(Bf)^{1.5} \tag{5}$$

where $\sigma_h$ is the hysteresis loss coefficient and $K_{ex}$ is the additional loss coefficient.

At the same time, the wires that flow through the current also generate a lot of heat, the direct current loss $P_{Al}$ of the wire is shown in Equation (6).

$$P_{Al} = \sum(I^2 R) \tag{6}$$

The motor consists of a stator and a rotor, which are separated by an oil-filled gap. As shown in Figure 3, the rotor and the permanent magnet undergo rotational motion, leading to the generation of viscous friction loss.
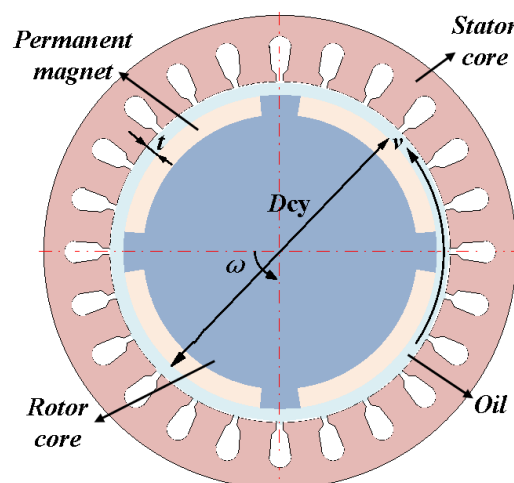


**Figure 3.** Schematic diagram of fluid domain between stator and rotor.

The mathematical model of viscous friction loss $P_{mj}$ of rotor under low-speed laminar flow and high-speed turbulence is shown in Equation (7) [10].

$$P_{mj} = \frac{\pi \mu \omega^2 l_{cy} D_{cy}^3}{4t} \tag{7}$$

where $l_{cy}$ and $D_{cy}$ are the length and diameter of the rotor, respectively, and $t$ is the spacing of the air gap.

The total motor power loss $P$ is shown in Equation (8).

$$P = P_b + P_h + P_{ex} + P_{Al} + P_{mj} \tag{8}$$

The connector between the high-pressure end of the pump and the low-pressure end of the motor results in throttling power loss when oil flows through it, as shown in Figure 4. The flow of oil can be simplified as the flow between annular gaps.
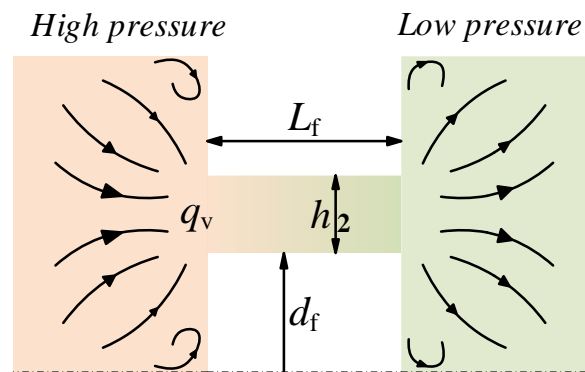


**Figure 4.** Diagram of connector.

The power loss $P_{zn}$ at the connector is shown in Equation (9).

$$p_{zn} = q_V \Delta p = \frac{12 \mu L_f q_V^2}{\pi d_f h_2{}^3} \tag{9}$$

where $q_v$ is the flow rate through the connector, $d_f$ is the diameter of the inner circle, $L_f$ is the gap length, $h$ is the gap width.

## 2.2. Heat Transfer Analysis

This paper employs the oil-immersed motor pump as a controlled object to regulate the energy conservation process, as shown in Figure 5.
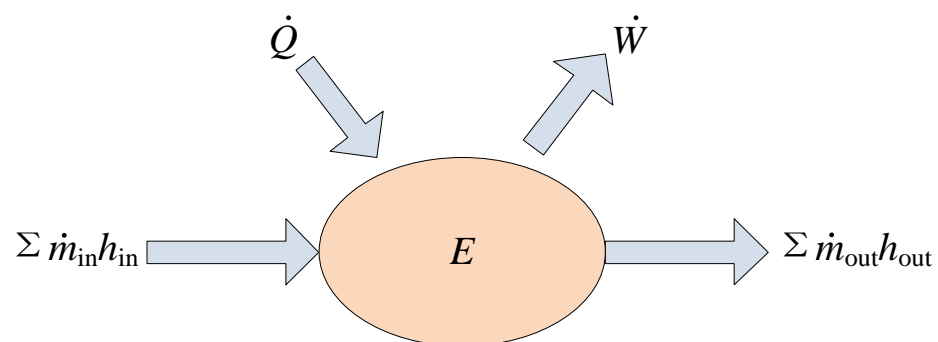


**Figure 5.** Control volume.

According to the first law of thermodynamics, the calculation formula is shown in Equation (10) [10].

$$\frac{dT}{dt} = \frac{1}{c_p m} [\sum \dot{m}_{in}(h_{in} - h) + \dot{Q} + mT\alpha_p v \frac{dp}{dt}]$$
$$h_{in} - h = \bar{c}_p(T_{in} - T) + (1 - \bar{\alpha}_p \bar{T})\bar{v}(p_{in} - p) \tag{10}$$

The figures depicting the heat transfer model of oil are presented in Figures 1 and 6. The motor pump model consists of five fluid nodes and one mass node; $T_p$ is the volume of

the outlet fluid, $T_t$ is the volume of the intake fluid. $T_b$, $T_j$ and $T_l$ are the volumes of the leakage fluid, and $T_w$ is the shell of the motor pump.
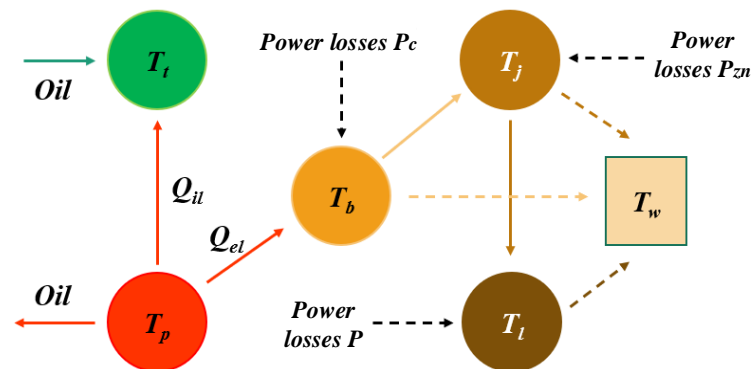


**Figure 6.** Thermodynamic nodal model.

The comprehensive thermodynamic calculation model of the pump is elaborately explained in Zhang's [10] article. Nevertheless, the focus of this paper is limited to the presentation of thermodynamic equations pertaining to the connector and leakage port nodes.

Oil with a flow rate of $Q_{el}$ is introduced into the motor via the connector located between the motor and the pump. The temperature of the oil is affected by the power loss occurring at the connector and subsequently rises to $T_j$, as shown in Equation (11).

$$
\begin{aligned}
\frac{dT_j}{dt} = {} & \frac{1}{c_p m_j} \left[ \rho Q_{el} \left( c_p (T_b - T_j) + (1 - \alpha_p (T_b + T_j)/2) v (p_b - p_j) \right) \right. \\
& \left. - k_{fw} A_{fw} (T_j - T_w) + p_{zn} + T_j \alpha_p V_j \frac{dp_j}{dt} \right]
\end{aligned}
\tag{11}
$$

The motor end receives an inflow of oil which is subsequently discharged via the leakage oil port. A considerable amount of heat is generated due to a succession of power losses occurring at the motor end, resulting in an increase in temperature at the leakage oil port, denoted as $T_l$ in Equation (12).

$$
\begin{aligned}
\frac{dT_l}{dt} = {} & \frac{1}{c_p m_l} \left[ \rho Q_{el} \left( c_p (T_j - T_l) + (1 - \alpha_p (T_j + T_l)/2) v (p_j - p_l) \right) \right. \\
& \left. - k_{fw} A_{fw} (T_l - T_w) + P + T_l \alpha_p V_l \frac{dp_l}{dt} \right]
\end{aligned}
\tag{12}
$$

The thermodynamic modeling of the oil-immersed motor pump is shown in Equation (13).

$$
\begin{cases}
\begin{aligned}
\frac{dT_t}{dt} = {} & \frac{1}{c_p m_t} \left[ \rho Q_{il} \left( c_p (T_p - T_t) + (1 - \alpha_p (T_p + T_t)/2) v (p_p - p_t) \right) \right. \\
& \left. + \frac{30}{\pi} c_p \rho \omega D (T_{in} - T_t) + T_t \alpha_p V_t \frac{dp_t}{dt} \right] \\
\frac{dT_p}{dt} = {} & \frac{1}{c_p m_p} \left[ \frac{30}{\pi} \rho \omega D \left( c_p (T_t - T_p) + (1 - \alpha_p (T_p + T_t)/2) v (p_t - p_p) \right) \right. \\
& \left. + \frac{30}{\pi} D \omega (P_p - P_t) + L_p + T_p \alpha_p V_p \frac{dp_p}{dt} \right] \\
\frac{dT_b}{dt} = {} & \frac{1}{c_p m_l} \left[ \rho Q_{el} \left( c_p (T_p - T_b) + (1 - \alpha_p (T_p + T_b)/2) v (p_p - p_b) \right) \right. \\
& \left. - k_{fw} A_{fw} (T_b - T_w) + P_c + T_b \alpha_p V_b \frac{dp_b}{dt} \right] \\
\frac{dT_j}{dt} = {} & \frac{1}{c_p m_j} \left[ \rho Q_{el} \left( c_p (T_b - T_j) + (1 - \alpha_p (T_b + T_j)/2) v (p_b - p_j) \right) \right. \\
& \left. - k_{fw} A_{fw} (T_j - T_w) + p_{zn} + T_j \alpha_p V_j \frac{dp_j}{dt} \right] \\
\frac{dT_l}{dt} = {} & \frac{1}{c_p m_l} \left[ \rho Q_{el} \left( c_p (T_j - T_l) + (1 - \alpha_p (T_j + T_l)/2) v (p_j - p_l) \right) \right. \\
& \left. - k_{fw} A_{fw} (T_l - T_w) + P + T_l \alpha_p V_l \frac{dp_l}{dt} \right] \\
\frac{dT_w}{dt} = {} & \frac{1}{c_w m_w} \left[ k_{fw} A_{fw} (T_b + T_j + T_l - 3T_w) \right. \\
& \left. - k_{wa} A_{wa} \left( (T_w + 273.15)^4 - (T_a + 273.15)^4 \right) \right]
\end{aligned}
\end{cases}
\tag{13}
$$

In the relevant research, the parameters of the plunger, cylinder block and valve plate are necessary [1]. And the main parameters of the motor are listed in Table 1.

**Table 1.** Main parameters of the motor.

| Parameter | Unit | Value |
|---|---|---|
| $B$ | T | 0.68 |
| $d$ | mm | 8.3 |
| $l$ | mm | 11.5 |
| $h$ | mm | 79 |
| $\sigma_h$ | W/(kg·Hz·T$^2$) | 0.136 |
| $k_{ex}$ | W/(kg·Hz$^2$·T$^2$) | 0.005 |
| $N$ | | 34 |
| $\rho_c$ | Ω·m | 0.0172 |
| $E$ | V | 270 |
| $D_{cy}$ | mm | 39 |
| $t$ | mm | 1 |
| $l_{cy}$ | mm | 79 |

### 2.3. Analytical Results

Due to the unfavorable flow characteristics of fluids at low speeds and high pressures, this paper aims to investigate the temperature variations of the leakage port and inlet at 1450 rpm under different outlet pressure conditions, as well as the temperature changes in the leakage port and inlet at different speeds when the outlet pressure is 6 MPa.

As shown in Figure 7a, an increase in the outlet pressure is observed to cause a gradual rise in the temperature of the leakage port. An increase in the temperature of the leakage port from a minimum of 25.1 to 41.2 °C is attributed to two factors. Firstly, an elevated viscous friction loss of oil is caused by an increase in pressure, resulting in a rise in the temperature of the oil that leaks into the motor pump. Simultaneously, an increase in motor power and current results in an elevated motor loss, further contributing to the rise in oil temperature at the leakage port. Nevertheless, the temperature of the inlet node remains constant., as the oil absorption rate at the inlet of the motor pump is significantly higher than the leakage rate. While some of the high-temperature oil may leak into the oil inlet, it does not significantly affect the overall temperature of the oil tank, and consequently, the temperature at the inlet remains relatively stable.
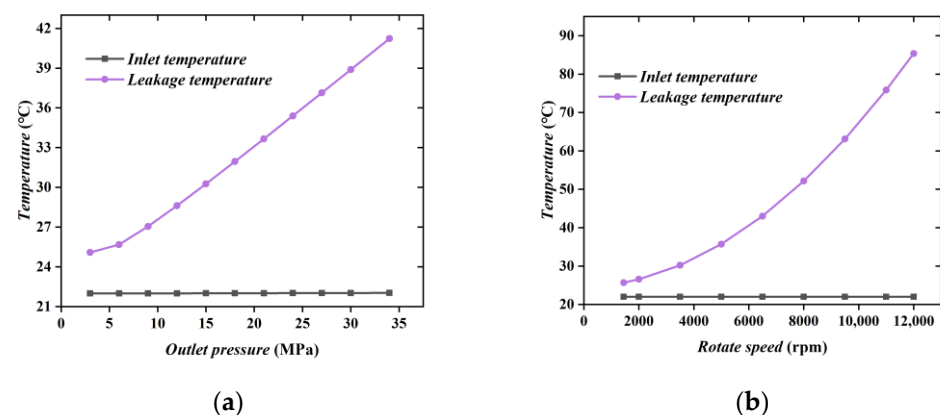


**Figure 7.** Temperature comparison under different loading conditions: (**a**) leakage and inlet temperature and under different load pressures; (**b**) leakage and inlet temperature under different rotation speeds.

As shown in Figure 7b, the temperature of the leakage port exhibits a gradual increment with escalating rotational speed. The temperature of the leakage port increases

gradually from an initial value of 25.7 °C to 85.4 °C, which can be attributed to two primary factors. As the rotational speed increases, the mixing loss of cylinder block, piston, and rotor intensifies, resulting in elevated levels of viscous friction loss within the pump chamber and motor chamber oil, thereby contributing to the increase in temperature of the leakage port. The rise in motor power and current translates to an amplified motor loss, consequently leading to a further escalation in oil temperature at the leakage port. Notably, the inlet temperature remains relatively unchanged owing to the increased heat exchange rate occurring between the inlet oil and exterior oil per unit time, which in turn preserves thermal equilibrium between the inlet temperature and the tank temperature.

## 3. Experimental Validations

Figure 8 shows the experimental picture of measuring the temperature of the motor pump. Port A and B are oil inlet and outlet, respectively.
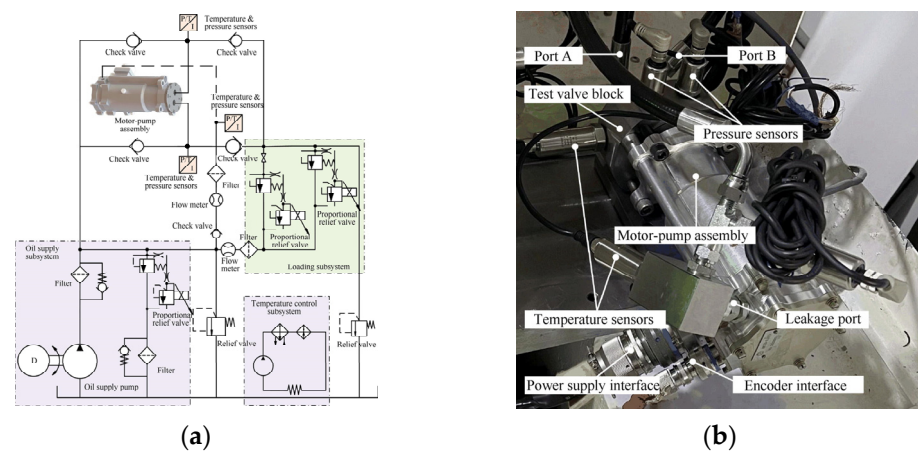


**Figure 8.** Principle and test system of the experiment [1]: (**a**) hydraulic principle diagram of test bench; (**b**) installation of the motor-pump assembly.

Ascertaining the temperature of the pump cavity and the connector node poses a challenge due to the sluggish balance temperature of the shell. Consequently, this study predominantly investigated the impact of motor loss on the overall temperature variation in the motor pump. Accordingly, the temperature of the inlet, outlet and leakage was measured in the conducted experiment. As shown in Figure 9, the temperature curve of the motor pump was depicted at 1450 rpm, measured at distinct outlet pressures. The solid line denotes the experimental value, while the calculated value is represented by the dashed line.
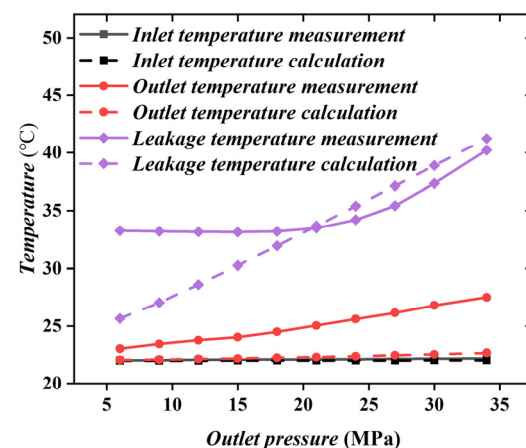


**Figure 9.** Comparison of measured and calculated temperature changes at each node with outlet pressure at 1450 rpm.

As shown in Figure 9, the experimental and calculated values of the inlet temperature remained consistent at approximately 22 °C and exhibited no changes throughout the operation of the motor pump. Conversely, the test temperature at the outlet experienced a surge of 4.86 °C, while the calculated temperature value displayed a minimal increment, albeit with an increasing trend. This phenomenon can be attributed to the escalating temperature rise of the overall system during the motor pump's operation. Notably, the calculated value deviates significantly from the experimental value under low pressure, with a maximum error of 22.79%. Nevertheless, as the pressure increases, the calculated value converges more closely to the experimental value.

Table 2 presents the maximum error values of the temperature at both the leakage port and outlet. The values listed in the upper section correspond to the case where the temperature at the leakage port is 6 MPa, while those in the lower section correspond to the case where the temperature at the outlet is 34 MPa. In this context, a represents the actual measured value, b denotes the corresponding calculated value, and c denotes the resulting error value.

$$c = \frac{|a - b|}{a} \tag{14}$$

**Table 2.** Value of the maximum temperature error of the leakage port and outlet.

| Measurement a | Calculation b | Error c |
|---|---|---|
| 33.26 °C | 25.68 °C | 22.79% |
| 27.52 °C | 22.67 °C | 17.7% |

Figure 10 illustrates the temperature curve of each node under distinct rotation speeds, with an outlet pressure of 6 MPa. The temperature of the inlet displays minor fluctuations, which can be attributed to variations in the ambient temperature. However, the temperature of the leakage port experiences an upsurge, primarily due to the increase in churning loss and motor power.
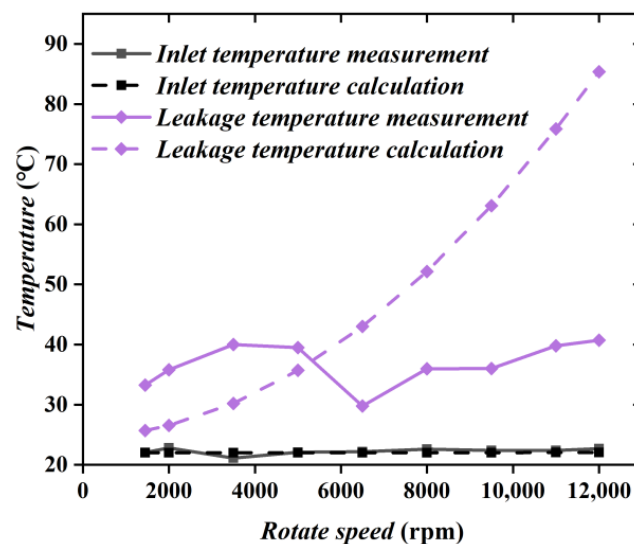


**Figure 10.** Comparison of measured and calculated temperature changes at each node with rotational speed under outlet pressure of 6 MPa.

The observed escalation in the leakage temperature, as determined through calculations, can be attributed to an exponential growth pattern. This phenomenon is predominantly a consequence of amplified heat generation resulting from heightened churning losses and motor power losses. Consequently, the system experiences a substantial temperature elevation of precisely 59.68 °C. The temperature measurements obtained displayed

a distinctive pattern characterized by an initial ascent, followed by a subsequent descent, and then another subsequent ascent. This observed behavior can be plausibly attributed to the impact of temperature variations on the rheological properties, specifically the viscosity, of the oil fluid. At lower rotation speeds, the higher viscosity of the oil fluid, attributed to lower temperatures, gives rise to pronounced friction losses, leading to relatively elevated temperatures. Nevertheless, as the rotational speed progressively increases, the viscosity of the oil fluid decreases, resulting in a subsequent temperature decline. However, as the rotational speed reaches a critical threshold, the impact of the viscosity changes becomes insufficient to counteract the fluctuations caused by interfacial viscous friction losses. Consequently, this leads to a subsequent temperature rise in the oil fluid. Under high-speed conditions, a substantial disparity is observed between the two measurements, with a maximum deviation of 109.7%. Nonetheless, both measurements demonstrate a convergent growth trend under these high-speed conditions.

The observed substantial disparities in calculation outcomes at high rotational velocities can be attributed to the inherent variability in oil viscosity resulting from the temperature elevation of the oil due to dynamic alterations in operating conditions. It should be noted that the preceding text solely accounted for a constant oil viscosity in the determination of the calculation results. The viscosity of Newtonian fluids exhibits a temperature-dependent behavior, whereby changes in temperature directly influence viscosity variations. However, due to the unavailability of initial temperature data, which is essential for predicting viscosity alterations, it becomes imperative to establish a correlation between viscosity and different rotational speeds and their corresponding outlet pressures. This empirical fitting process is illustrated in Figure 11.
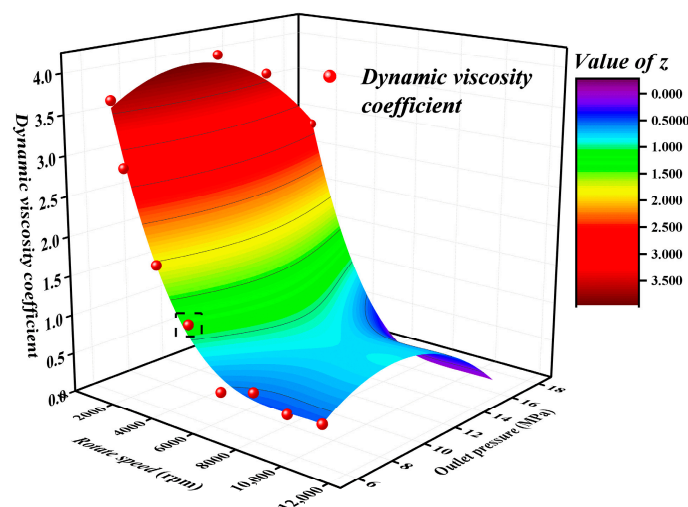


**Figure 11.** Fitted surface of viscosity coefficient for oil fluids.

Regarding the global fitting surface, the dynamic viscosity coefficient demonstrates a decreasing trend with increasing rotational speed, exhibiting a quadratic relationship. It initially starts at a value of 3.695 and progressively decreases to 0.496. As the pressure increases, the dynamic viscosity coefficient displays an initial ascending trend followed by a descending trend. The maximum value of 4.01 is observed at 12 MPa, while the minimum value of 2.82 is observed at 18 MPa. Equation (15) defines the fitting equation, wherein $x$ represents the rotational speed in rpm (revolutions per minute), $y$ represents the outlet pressure in MPa (megapascals), $z$ symbolizes the dimensionless viscosity coefficient, and $\mu_1$ is the dynamic viscosity after fitting. In Figure 12, the circled temperature is 39.4 °C, and the viscosity coefficient $z$ is close to 1. There is a small difference between the corresponding

viscosity value at 33.7 °C and the standard value, which indicates the correctness of the fitting surface.

$$
\begin{aligned}
z &= 3.95217 - 0.00157x + 1.61409 \times 10^{-7}x^2 - \\
&\quad 5.48032 \times 10^{-12}x^3 + 0.37877y - 0.0183y^2 \\
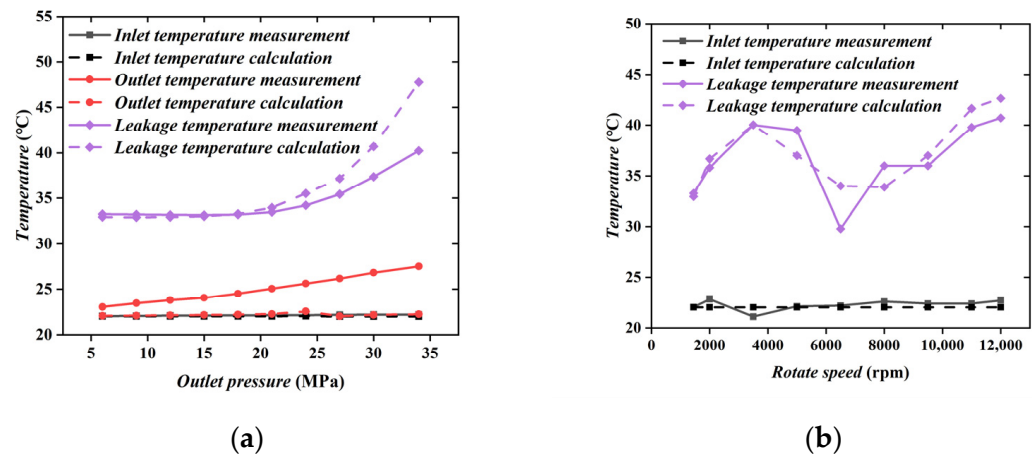\mu_1 &= z\mu
\end{aligned}
\tag{15}
$$



**Figure 12.** Temperature comparison of the fitted dynamic viscosity: (**a**) leakage and inlet temperature and under different load pressures; (**b**) leakage and inlet temperature under different rotation speeds.

The viscosity values, recalculated by substituting the fitted viscosity coefficients, are employed in subsequent computations. The outcomes of these calculations are illustrated in Figure 12. Within Figure 12a, the leakage port temperature exhibits a relatively stable profile within the pressure range of 3–18 MPa. However, beyond this range, specifically within the 18–34 MPa pressure interval, the temperature demonstrates an exponential increase. Notably, the calculated values exhibit a parallel trend in variation to the measured values, indicating a comparable pattern. At low pressures, the calculated and actual values of the leakage port oil temperature exhibit a remarkable level of agreement, indicating a high degree of fitting. However, at high pressures, there is a comparatively larger deviation between the calculated and actual values. For the purpose of ensuring precise calculations, the subsequent text will exclusively focus on the temperature fluctuations at different nodes associated with outlet pressures ranging from 3 to 18 MPa.

As depicted in Figure 12b, the calculated values exhibit a trend of variation similar to that of the measured values. The temperature follows a pattern characterized by an initial increase with rotational speed, followed by a subsequent decrease, and then a subsequent increase. The underlying mechanism can be explained as follows: with an increase in rotational speed, the churning losses intensify, resulting in an escalation of viscous friction losses between the oil molecules, consequently leading to an elevation in temperature. However, as the temperature surpasses a certain threshold, the viscosity of the oil decreases, leading to a reduction in the viscous friction losses between the oil molecules, which in turn causes a decline in temperature. At 6500 rpm, the temperature reaches its minimum value and the maximum error is 14.1%. Subsequently, the further decrease in oil viscosity caused by the increase in rotational speed fails to counteract the amplified viscous friction losses between the oil molecules, resulting in an upward trend in temperature.

Figure 13 shows the loss value of the motor when the outlet pressure is 6 MPa, and the six loss values of the motor are similar at low speed, while the power loss of the motor increases with the increase in speed; stirring loss Pal and resistance loss increase most obviously, and the two values are relatively close.
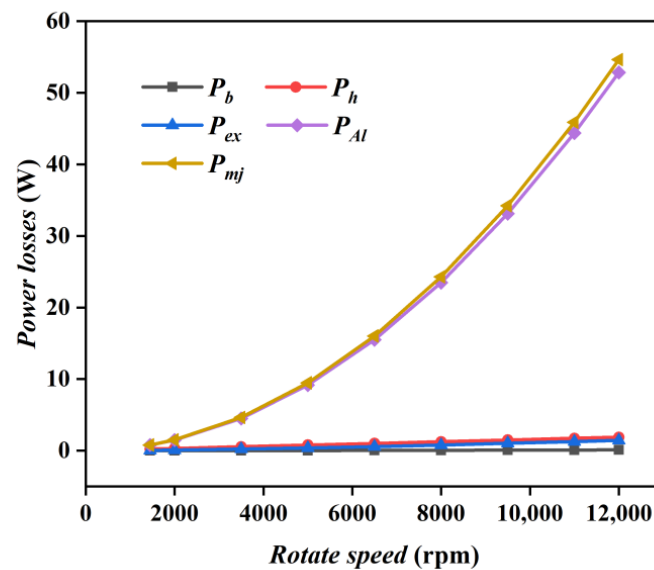
**Figure 13.** Calculated loss under 6 MPa outlet pressure.

## 4. Discussion

Considering the negligible discrepancy observed between the calculated leakage temperature and the corresponding actual temperature, the thermodynamic model utilized in this study is demonstrated to possess high accuracy. Therefore, the investigation is further expanded to incorporate a more comprehensive range of operating conditions.

Figure 14 depicts the temporal evolution of individual nodes in the context of a motor pump operating at a speed of 1450 rpm and an outlet pressure of 6 MPa. To be specific, the temperature of the inlet, outlet, leakage port, and connector node all exhibit an upward trajectory, beginning simultaneously from their respective initial values. After approximately 20,000 s of operation, the temperature of each node ultimately attains a steady-state condition. The temperature attained at the leakage port, connector, pump chamber, and shell were recorded as 26.5, 27.1, 32.9, and 27.6 °C, respectively. It is noteworthy that the temperature of the inlet and outlet nodes is observed to be nearly identical, with the outlet temperature being only 0.05 °C higher than that of the inlet. Furthermore, owing to the distinctive radiative heat transfer process that occurs through the surrounding air, the temperature of the shell undergoes a relatively slow and gradual stabilization process.
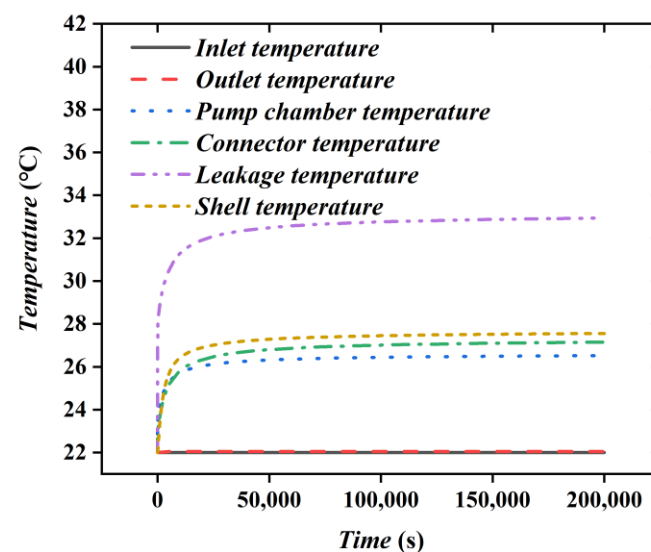


**Figure 14.** Temperature change curves of each node at 1450 rpm and 6 MPa.

The temperature readings in Figure 15 reveal that the inlet, outlet, leakage outlet, shell, pump chamber and connector experienced, respectively, temperature increments of 0.04, 0.2, 0.4, 2.2, 5.1 and 3.7 °C. The rise in outlet temperature corresponds to an increase in outlet pressure, which induces a higher input torque, thus augmenting the external input power to the pump and elevating the outlet temperature. Meanwhile, the inlet temperature elevation arises from heightened heat leakage from the outlet into the inlet, raising the temperature of the inlet oil. Furthermore, the increase in motor power and the change in oil viscosity cause the temperature of the leakage port to change. Lastly, as the oil temperature within the motor pump escalates, the temperature of the shell increases, given that the contact area and heat transfer coefficient between the shell and the oil remain constant.
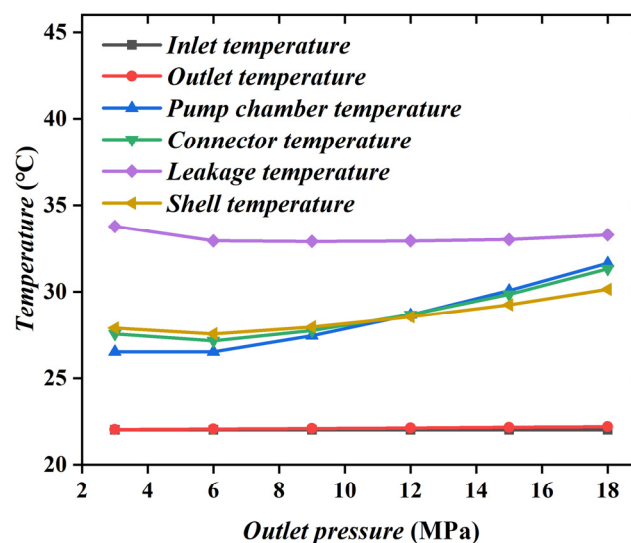


**Figure 15.** The temperature curve of each node varies with the outlet pressure at 1450 rpm.

As the outlet pressure is increased, there is a trend towards temperature equalization observed between the pump chamber, connector, and leakage port. The rise in outlet pressure results in an elevation of the pump oil leakage rate, which in turn increases the influx of oil into the pump chamber, connector, and leakage port, ultimately leading to an accelerated rate of heat exchange between the motor pump and its internal components. Consequently, this dynamic process causes the temperature distribution within the motor pump to become more uniform. As the outlet pressure is raised, there is a more linear and progressive increase observed in the temperature of each connector.

Figure 16 illustrates that the temperatures of the inlet and outlet nodes remain stable, exhibiting minimal fluctuations over time. The temperature change follows a specific order, with the highest temperature change occurring at the leakage port, followed by the connector, pump chamber, shell, oil outlet, and oil inlet nodes. The temperature change values of each node are 9.7, 2.7, 2.3 and 1.6 °C, respectively. As the rotational speed increases, the temperature demonstrates a non-linear variation characterized by an initial rise, followed by a decline, and then a subsequent rise. This behavior primarily arises from the consequential impact of temperature fluctuations on the viscosity of the oil fluid. The similarity observed in temperature changes between the pump chamber and the connector can be attributed to the influence of throttling losses on the pump chamber and the heat generated through viscous friction between the oil fluids. The small temperature difference between the connector and the pump chamber indicates that the effect of connector throttling loss is negligible. The observed elevation in oil temperature can be predominantly ascribed to churning losses resulting from high-velocity lubricating oil at the leakage end, accompanied by a subsequent escalation in motor power losses. This underscores the notable significance of temperature increment induced by the electric motor, warranting careful consideration.
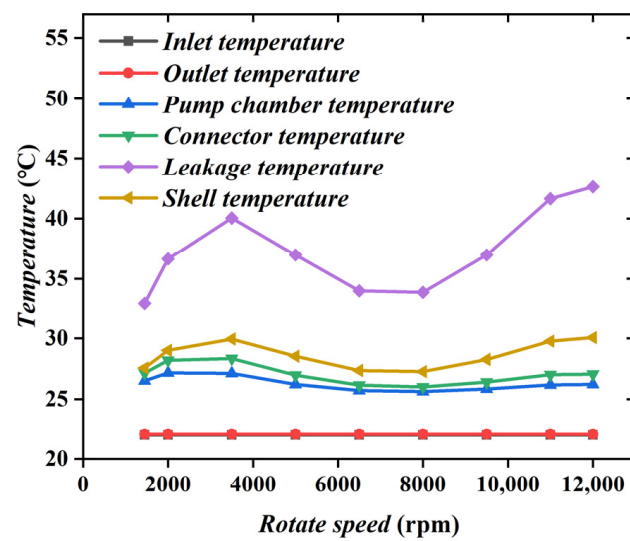
**Figure 16.** Temperature curve of each node varies with the rotating speed at outlet pressure of 6 MPa.

As shown in Figure 17, the leakage port oil temperature across different operational scenarios is calculated. At low pressure conditions, the oil temperature remains within an acceptable range. However, as the pressure and rotational speeds increase, limitations become evident. This is primarily due to the fact that under high-pressure and high-speed conditions, the oil fluid temperature is more prone to reaching elevated levels. Consequently, this leads to a deterioration in the overall performance of the motor pump system. At a pressure of 9 MPa, the temperature is relatively elevated. However, it is important to highlight that a critical threshold is observed at a pressure of 15 MPa. At this critical point, a transition occurs in the oil temperature regime, shifting from higher temperatures to lower temperatures.
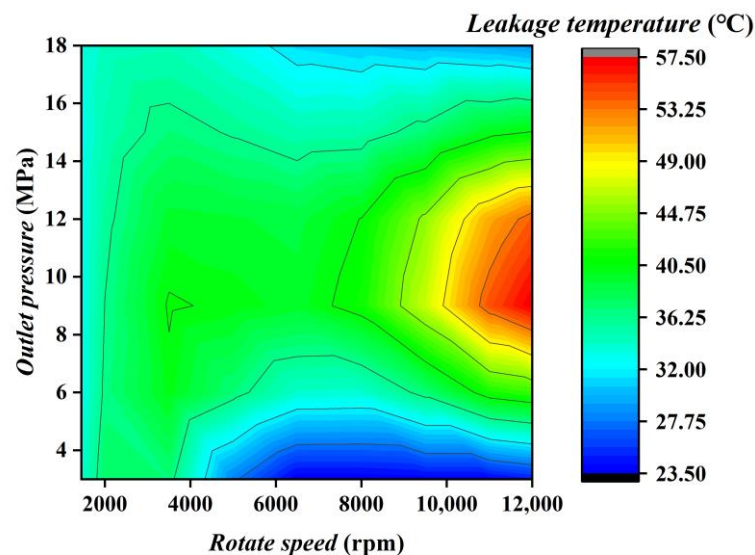


**Figure 17.** The dynamic evolution of oil fluid temperature at the leakage across the entire range of operating conditions.

As shown in Figure 17, the calculated values of oil temperature at the leakage point under various operating conditions are shown in the diagram. At low pressure, the oil temperature remains within a reasonable range, with a maximum temperature of 57.5 °C. However, at 8–12 MPa, the temperature shows an increasing trend with higher rotational speeds, while at other pressures, it exhibits a decreasing trend followed by an increase. This is mainly because the leakage of oil at 3–8 MPa gradually increases, leading to an

increase in heat exchange efficiency between the oil, resulting in temperature reduction. However, as the rotational speed increases, motor losses such as churning losses also increase, causing the temperature to rise. At 12–18 MPa, the continuous temperature increase causes a decrease in oil viscosity, which in turn leads to temperature reduction. However, with the continuous increase in motor losses, the temperature variation caused by viscosity no longer suppresses the temperature rise caused by the motor. At a constant rotational speed, the temperature exhibits a trend of initially increasing and then decreasing. At a pressure of 9 MPa, the temperature is relatively high. However, it is worth noting that at a pressure of 15 MPa, it is the critical value where the oil temperature begins to transition from high to low. In conclusion, the variation in oil temperature is influenced by the leakage amount of oil flowing inward, oil viscosity, and motor losses, which all contribute to these changes.

As shown in Figure 18a, when the outlet pressure condition is changed, it is observed that the temperature change with motor power loss is more than 2.8 °C than that without motor power loss. This observation highlights the significant impact of motor power loss on the resultant changes in oil viscosity. In low-pressure conditions, a distinct temperature disparity is observed between scenarios with motor power loss and without motor power loss. However, as the pressure rises, the temperature gap between the two scenarios diminishes, and the temperature response tends towards linearity. This phenomenon can be ascribed to the similarity in oil viscosity corresponding to these temperature levels. Additionally, under higher pressures, the oil leakage rate experiences a substantial increase, leading to accelerated heat exchange at the leakage port. Consequently, the temperature tends to converge towards a state resembling that of no motor power loss.
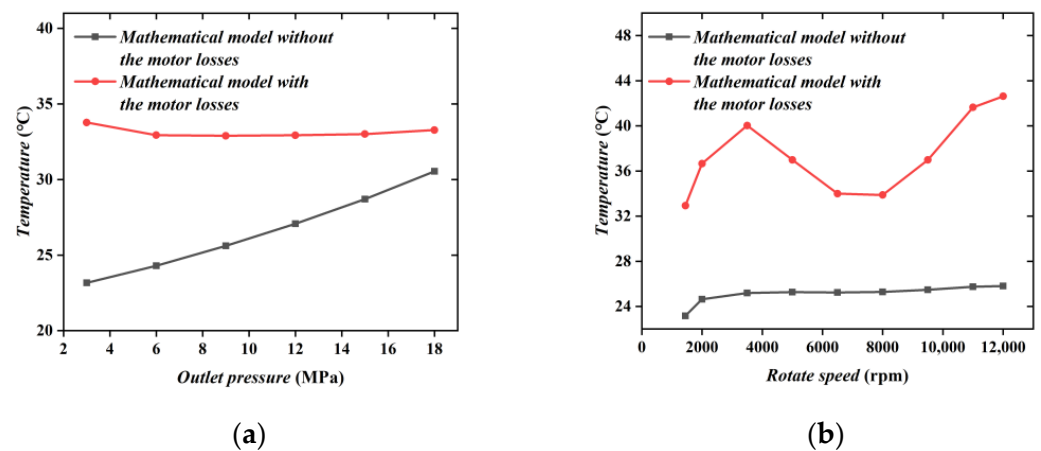


**Figure 18.** Temperature comparison under different loading conditions: (**a**) leakage temperature under different load pressure; (**b**) leakage temperature under different rotation speeds.

As shown in Figure 18b, when considering changes in rotational speed, it can be observed that the temperature increases by 9.7 and 2.6 °C due to motor power loss and non-motor power loss, respectively. In general, there exists a notable disparity in temperature between the two scenarios, with the maximum temperature differential observed at 12,000 rpm, reaching 16.8 °C. However, at higher rotational speeds, the impact of churning losses becomes more pronounced, leading to a more conspicuous temperature elevation at the leakage port. Hence, the influence of motor power loss should not be underestimated, as it can result in a substantial escalation of leakage temperature, particularly during operations involving high-speed rotation.

## 5. Conclusions

This paper took the integrated oil-immersed motor pump as the research object, and carried out research work in three aspects: loss source of motor, thermodynamic modeling, and experimental verification. The heat generation mechanism of the motor

was analyzed, and a thermodynamic model suitable for the integrated oil-immersed motor pump was established. The accuracy of the thermodynamic model was demonstrated through experiments. The research results are as follows:

(1) In this paper, the heat generation mechanism of the oil-immersed motor pump was analyzed, and the mathematical models of the copper and iron consumption of the motor, the churning loss of the rotor and the throttling loss of the damping hole were established.

(2) The influence of rotational speed and outlet pressure on the temperature of each node was verified by experiments, and the fitted equation capturing the variation in oil fluid viscosity with operating conditions was established. The viscosity coefficient was close to 1 when the measured temperature was 39.4 °C. Upon applying the fitted equation, the maximum error between the calculated value and the experimental data was 14%, thereby validating the accuracy of the thermodynamic model for oil-immersed motor pumps.

(3) Based on the conservation of energy theory, a thermodynamic model for the oil-immersed motor pump was established and solved and the temperature variation in key nodes with time was obtained. Each node reached equilibrium in 20,000 s, and the temperature of the leakage port was the highest, reaching 32.9 °C. At the same time, the influence of pressure and rotating speed on the heat-balance temperature of the oil-immersed motor pump was analyzed. The temperature of the oil at the leakage port exhibited a non-linear relationship with the working condition, displaying a distinctive pattern of initial ascent followed by descent. The peak temperature recorded was measured at 57.5 °C. Subsequently, temperatures at higher pressures and rotational speeds were tested to determine the expected final operating state.

**Abbreviations**

| | |
|---|---|
| $P_b$ | eddy current loss of the iron core |
| $P_h$ | hysteresis loss of the iron core |
| $P_{ex}$ | extra loss of the iron core |
| $P_w$ | alternating current loss of the wire |
| $P_{Al}$ | direct current loss of the wire |
| $P_{mj}$ | viscous friction loss of rotor |
| $P_{zn}$ | power loss of the connector |
| $P$ | total motor power loss |
| $f$ | frequency |
| $\rho_1$ | resistivity |
| $B$ | flux density |
| $d$ | thickness of the steel sheet |
| $l$ | length of the steel sheet |
| $h$ | height of the steel sheet |
| $\sigma_h$ | hysteresis loss coefficient |
| $K_{ex}$ | additional loss coefficient |
| $\mu_0$ | permeability of air |
| $\omega_1$ | angular frequency |
| $d_1$ | diameter of conductor |
| $N$ | number of conductors |
| $I$ | current intensity |
| $l_1$ | length of conductor |
| $\rho_c$ | resistivity of a conductor |
| $b$ | width of groove |
| $h_1$ | depth of groove |
| $R$ | resistance of conductor |
| $\mu$ | viscosity of the oil |
| $\omega$ | angular velocity |
| $l_{cy}$ | length of rotor |
| $D_{cy}$ | diameter of rotor |
| $t_4$ | oil gap |
| $\rho$ | density of oil |
| $L_f$ | length of the damping hole |
| $d_f$ | diameter |
| $h$ | width of the damping hole |

**References**

1. Zhao, J.; Fu, J.; Li, Y.; Qi, H.; Wang, Y.; Fu, Y. Flow characteristics of integrated motor-pump assembly with phosphate ester medium for aerospace electro-hydrostatic actuators. *Chin. J. Aeronaut.* **2022**. [CrossRef]
2. Liu, Y.; Mo, D.; Nalianda, D.; Li, Y.; Roumeliotis, I. Review of More Electric Engines for Civil Aircraft. *Int. J. Aeronaut. Space Sci.* **2022**, *23*, 784–793. [CrossRef]
3. Guo, S.; Chen, J.; Lu, Y.; Wang, Y.; Dong, H. Hydraulic piston pump in civil aircraft: Current status, future directions and critical technologies. *Chin. J. Aeronaut.* **2020**, *33*, 16–30.
4. Ehresman, J.D. Integration of Actuators and Sensors into Composite Structures. Ph.D. Thesis, College of Engineering, Montana State University-Bozeman, Bozeman, MT, USA, 2009.
5. Chao, Q.; Xu, Z.; Tao, J.; Liu, C. Capped piston: A promising design to reduce compressibility effects, pressure ripple and cavitation for high-speed and high-pressure axial piston pumps. *Alex. Eng. J.* **2023**, *62*, 509–521. [CrossRef]
6. Arkadan, A.A.; Vyas, R.; Vaidya, J.; Shah, M. Effect of toothless stator design and core and stator conductors eddy current losses in permanent magnet generators. *IEEE Trans. Energy Convers.* **1992**, *7*, 231–237. [CrossRef]
7. Inderka, R.B.; Carstensen, C.; De Doncker, R. Eddy currents in medium power switched reluctance machines. In Proceedings of the 2002 IEEE 33rd Annual IEEE Power Electronics Specialists Conference. Proceedings (Cat. No. 02CH37289), Cairns, QLD, Australia, 23–27 June 2002; pp. 979–984.
8. Mellor, P.H.; Wrobel, R.; McNeill, N. Investigation of proximity losses in a high speed brushless permanent magnet motor. In Proceedings of the Conference Record of the 2006 IEEE Industry Applications Conference Forty-First IAS Annual Meeting, Tampa, FL, USA, 8–12 October 2006; pp. 1514–1518.

9.	Wang, R.-J.; Kamper, M.J. Calculation of eddy current loss in axial field permanent-magnet machine with coreless stator. *IEEE Trans. Energy Convers.* **2004**, *19*, 532–538. [CrossRef]

10.	Zhang, J.; Li, Y.; Xu, B.; Chen, X.; Pan, M. Churning losses analysis on the thermal-hydraulic model of a high-speed electro-hydrostatic actuator pump. *Int. J. Heat Mass Transf.* **2018**, *127*, 1023–1030. [CrossRef]

11.	Shi, G.; Wang, H. Thermal-hydraulic model for axial piston pump with leakage and friction and its application. *Ind. Lubr. Tribol.* **2019**, *71*, 810–818. [CrossRef]

12.	Jordan, H. Die ferromagnetischen Konstanten für schwache Wechselfelder. *Elektr. Nach. Technol.* **1924**, *1*, 8.

13.	Bertotti, G. Direct relation between hysteresis and dynamic losses in soft magnetic materials. *Le J. Phys. Colloq.* **1985**, *46*, C6-389–C6-392. [CrossRef]

14.	Bertotti, G. General properties of power losses in soft ferromagnetic materials. *IEEE Trans. Magn.* **1988**, *24*, 621–630. [CrossRef]

15.	Gao, D.; Zhang, Z.; Sun, Y.; Xu, S.; Liu, J.; Zhang, Y. Numerical simulation and analysis of temperature and flow field of high-speed axial piston motor pump. *J. Eng.* **2019**, *2019*, 127–131. [CrossRef]

16.	Li, Z.; Wang, P.; Liu, L.; Xu, Q.; Che, S.; Zhang, L.; Du, S.; Zhang, H.; Sun, H. Loss calculation and thermal analysis of ultra-high speed permanent magnet motor. *Heliyon* **2022**, *8*, e11350. [CrossRef] [PubMed]

17.	Popescu, M.; Dorrell, D.G.; Alberti, L.; Bianchi, N.; Staton, D.A.; Hawkins, D. Thermal analysis of duplex three-phase induction motor under fault operating conditions. *IEEE Trans. Ind. Appl.* **2013**, *49*, 1523–1530. [CrossRef]

18.	Lu, Q.; Zhang, X.; Chen, Y.; Huang, X.; Ye, Y.; Zhu, Z. Modeling and investigation of thermal characteristics of a water-cooled permanent-magnet linear motor. *IEEE Trans. Ind. Appl.* **2014**, *51*, 2086–2096. [CrossRef]

19.	Guo, H.; Lv, Z.; Wu, Z.; Wei, B. Multi-physics design of a novel turbine permanent magnet generator used for downhole high-pressure high-temperature environment. *IET Electr. Power Appl.* **2013**, *7*, 214–222. [CrossRef]

20.	Tinni, A.; Knittel, D.; Nouari, M.; Sturtzer, G. Electrical–thermal modeling of a double-canned induction motor for electrical performance analysis and motor lifetime determination. *Electr. Eng.* **2021**, *103*, 103–114. [CrossRef]

21.	Wang, S.; Luo, G.; Shen, H.; Yao, Z. Heat transfer behavior of the boundary layer near surfaces in annular flow of high capacity canned motor pump. In Proceedings of the ASME International Mechanical Engineering Congress and Exposition, American Society of Mechanical Engineers, Phoenix, AZ, USA, 11–17 November 2016; p. V008T010A056.

22.	Elhomdy, E.; Liu, Z.; Li, G. Thermal and mechanical analysis of a 72/48 switched reluctance motor for low-speed direct-drive mining applications. *Appl. Sci.* **2019**, *9*, 2722. [CrossRef]